Kufa Journal of Engineering
Vol. 17, No. 2, April 2026, P.P. 292-309
Article history: Received 13 May 2025, last revised 23 July 2025, accepted 17 July 2025

MULTI-SEASONAL LAND COVER CLASSIFICATION THROUGH INTEGRATION OF SENTINEL-1 AND 2 DATA WITH SERIAL CELLS FROM LSTM: KARBALA CASE STUDY

Safaa Hadi Kother [1] and Hadab Khalid Obayes [2]

[1] College of Information Technology, University of Babylon, Babylon, Iraq, Email:safaahk.sw.phd@student.uobabylon.edu.iq.

[2] College of Education for Humanities Studies, University of Babylon, Babylon, Iraq, Email:hedhab@uobabylon.edu.iq.

https://doi.org/10.30572/2018/KJE/170217

ABSTRACT

With significant technological advancements, deep learning models have become powerful and essential tools for image classification and object recognition, particularly in classifying land cover images captured by satellite sensors. However, these models require a substantial amount of high-quality training data. This study introduces a novel strategy for enhancing and increasing the size of the time series of training samples. Zonal statistics are used to eliminate class contamination within the buffer area. This research aims to utilize time series data and select suitable bands to improve classification accuracy through multiple Long Short-Term Memory (LSTM) cells. By integrating data from Sentinel-1 (S1) and Sentinel-2 (S2) sensors, the study provides comprehensive insights for the research area of Karbala City, Iraq. The results demonstrated that the proposed system achieved high accuracy compared to prior studies, the overall accuracy reaching 98.66% and 96.75% for the Kappa coefficient by using zonal statistics.

KEYWORDS

Remote Sensing (RS), Land Cover (LC) Classification, Sentinel-1 (S1), Sentinel-2 (S2), Long Short-Term Memory (LSTM), Zonal Statistics (ZS), Time series data.

1. INTRODUCTION

Countries need data on changes in Land Use and Land Cover (LULC) to monitor land changes over time (Almeida et al., 2016). This information enables the monitoring of protected areas, quantifying deforestation in tropical regions and assessing the impact of urban expansion on all ecosystems (Wang et al., 2018; Sannigrahi et al., 2018) .In today's world remote sensing has become very important. It supports and assists human beings in many fields, including LULC hydrology agriculture as well as environmental monitoring. Remote sensing contributes to the development of a country by category and monitoring land utilization as well as recognizing issues in risky or inaccessible areas (Yassine, Tout and Jaber, 2021). Researchers struggle to give the most correct land cover maps, which can offer great information and help us know how to use natural and geographical resources (Choudhury et al., 2023). Thus, accurate land cover class is key for the management of land and getting good watch as well as warning about geographic hazards (Acharya, Hori and Karki, 2023).

The Sentinel mission works for all fields of science (Dagne et al., 2023).The optical/multispectral Sentinel-2 (S2) picture has shown good use in several activities that include mapping cities, recognizing burned areas, mapping minerals changed by hydrothermal alteration, and finding the chance of landslides (Roteta et al., 2019; Hu et al., 2018).But putting water and dark, hard surfaces into groups is a big problem because they look very much the same. So it is not easy to put into the right group using just S2 data as dark unbreakable surfaces may be seen as water leading to wrong understanding (Zhang et al., 2018). Applications delivered by Sentinel-1 (S1) Synthetic Aperture Radar (SAR) imaging are manifold. Land cover mapping, crop monitoring, soil moisture retrieval, and rice production estimation are among the more popular applications (Ruzza et al., 2019; Bao et al., 2018). It is here that it should be noted that S1 SAR images can serve as a valid surrogate for quality S2 images in cases where they come to be compromised by fog or cloud cover. The rapid generation of land cover maps via S1 SAR is very instrumental in enhancing urban management efficiency imagery. Accurate land cover classifications using S1 SAR data have, however, been impeded by the puzzling assemblages of material distributions within the urban environment. S1 and S2 data fusion are being explored by researchers to ameliorate these challenges in classification outputs. The fusion method has been used successfully for applications concerning vegetation type classification, forest biomass estimation, and burned area mapping (Erinjery, Singh and Kent, 2018; Colson, Petropoulos and Ferentinos, 2018). Thus improved perspectives and consistent results for various applications can be obtained when combining unique properties from both S2 and S1 datasets (Mahdianpari et al., 2019). These fuse data need preprocessing steps to

enhance the images to usable forms for different models (Nigar et al., 2024). An important step in the preprocessing stage is to remove clouds from the raw image by using the previously proposed cloud masking technique by (Zurqani et al., 2022). The step about how many bands to use as mentioned in (Kother and Obayes, 2025), and spectral indices is also very important (Lunetta et al., 2006).The researchers developed several methodologies to deal with the LULC classification challenges. Among the techniques are the use of Deep Neural Network (DNN), which falls under a broader concept known as Artificial Neural Network (ANN)(Mohammed, Kareem and Mohammed, 2022), an adaptive reflectance fusion model, decision tree, and maximum likelihood classifier (Rajendran et al., 2020). Conventional interpretation techniques applied in LULC classification are greatly influenced by factors such as the destruction of essential marshes, arbitrary urbanization, degradation of ecological quality, and factors like cloud cover and regional fog mistakes.

The Long Short Term Memory (LSTM) deep learning models have performed very well or rather succeeded in the task of classification of land cover by discerning temporal patterns from a series of satellite images (H, 2024), (Rajendran et al., 2020). The hybrid approach to feature optimization based on a deep learning classifier is discussed in (Rajendran et al., 2020). Features are extracted using Haralick texture features, a histogram of directed gradients, and a sequence of Gabor local binary pattern histograms. Classification is carried out using an LSTM network (alsraratee and Al-Azawei, 2025), while feature selection is executed with the help of human-based particle swarm optimization. A method has been proposed in (Tejasree and Agilandeeswari, 2024) for classifying LULC from hyperspectral images acquired via remote sensing based on deep-Long Short-Term Memory (deep-LSTM), which requires relevant bands to be selected together with the extraction of useful features. It consists mainly of an auto-encoder model used for feature extraction, a band selection model based on ranking, and a deep-LSTM used for classification. The procedure performs better in terms of accuracy compared to other state-of-the-art techniques.

The method proposed by (Santos et al., 2021) uses Self-Organizing Maps with Bayesian inference to evaluate within-cluster and between-cluster similarities in the cause of imagery and identify noisy samples as outliers so that all quality of time series satellite imagery can be improved. This method proved very effective toward reducing class noise. Several methods and strategies regarding enhancement pertaining- to both the size and quality of data for the insufficiency problem of training datasets in deep learning networks, discussed by (Shorten and Khoshgoftaar, 2019), have been made better building deep learning models more accurate. Current methods were emphasized which are under promising development regarding the

implementation as well as activation of the role of data augmentation. It underscored how it can bring about an improvement in the effectiveness of models utilized on classification.

This study presents a buffer-based data enhancement method that is used in generating training samples through the aggregation of multi-temporal pixel neighborhoods so as to guarantee a richer spatial-temporal representation. One major problem with buffer-based methods is class overlapping within the buffer zones, which results in model accuracy degradation. Existing works such as (Ienco et al., 2017) introduced ConvLSTM for handling spatial-temporal correlations but did not consider noise induced from buffers. Here, the statistics-based mechanism is proposed to mitigate class interference by analyzing pixel-wise spectral statistics (e.g., mean, variance) within buffers, thereby preserving class separability. This approach aligns with (Santos et al., 2021), who emphasized handling noise reduction in optical remote sensing time series, but extends it to dynamic buffer surrounds.

2. MATERIALS AND METHODS

2.1. Study Area

Karbala, which lies geographically between longitudes 44.0197° E east and latitudes 32.6027° N north, was chosen for the current study. It is positioned in the center of Iraq, 110 kilometers southwest of Baghdad, the capital, Fig.1 illustrates a map of the study area's location. It borders the province of Anbar to the north and west, Babel to the east, and Najaf to the south. Approximately 5034 km2 make up the Karbala province, or 1.2% of the 434,934 km2 total area of Iraq. This location faces challenges because of its desert borders, particularly to the west, which makes it difficult for cities to connect with other areas. However, the city benefits from its natural surroundings, which include notable agricultural and tourism destinations nearby, known for their abundance of palm fields, fruits, and vegetables. Because it mostly consists of water bodies, urban areas, palm trees, agricultural land, and bare land, this research area was selected. Furthermore, the city includes Lake Razaza, one of Iraq's most natural lakes, which is situated around 11 km northwest.

2.2. Dataset

For the LULC classification procedures, creating the basic dataset is essential. The dataset includes a time-series of S1 and S2 images captured in 2024 across four seasons, along with three multispectral image indices: normalized difference vegetation index (NDVI), normalized difference water index (NDWI), and normalized difference built-up index (NDBI). Data from S1 obtained in Interferometric Wide Swath Mode (IW) from the European Space Agency (ESA). This collection features S1 Ground Range Detected (GRD) scenes and offers 10 m

spatial resolution. The S1 mission produces information in a descending and ascending mode in two polarization forms at the VH and VV bands. The time series of S1 filtered based on the orbit aspect (descending or ascending mode), then the number of descending or ascending tiles computed, and the one with the most tiles was used. Fig.2a illustrates an S1 image for Karbala city was created with VV and VH bands in ascending mode and VH band in descending mode from means at different look angles and polarizations. Table 1 describes S1 band information. The S2 mission, with multispectral bands, also obtained from the ESA. The cloud masking technique is applied to be analyzed and classified. Fig.2b illustrates an S2 image.

Sentinel-2 imagery including 13 spectral bands from 443 to 2190 nm. The key bands are taken at a spatial resolution of 10 meters (B2, B3, B4, B8) and at 20 meters (B5, B6, B7, B8A, B11, B12). Additionally, three spectral index bands (NDVI, NDWI, and NDBI) support this data. As in Table 2, for a concise summary of the data used in the study area.

The final composite image produced with 16 bands (B2, B3, B4, B5, B6, B7, B8A, B8, B11, B12, NDVI, NDWI, NDBI, VV, VH, VH_1), as shown in Fig.2c. The ROI mask applied to the final composite image, and 300 sample points selected, 60 for each class in LULC types.

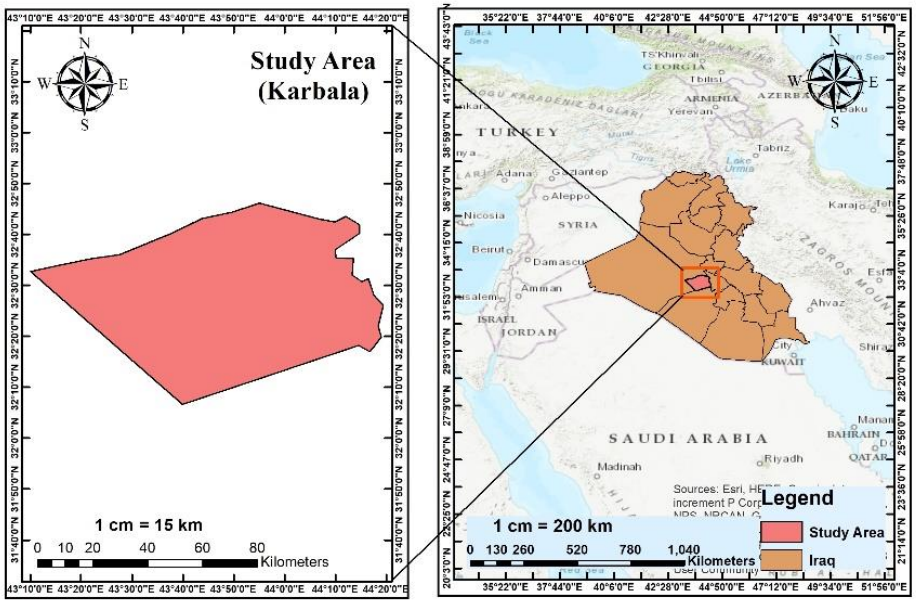

Fig. 1. Map illustrating the study area's location

Table 1. Description of S1 bands information

Bands	Description	Spatial resolution (m)
HH	Single co-polarization, horizontal transmission/horizontal reception	10
HV	Cross-polarized dual-band transmission with horizontal send and vertical receive.	10
VV	Single co-polarization, vertical transmission, and vertical reception	10
VH	Dual-band cross-polarization with vertical transmission and horizontal reception	10

Table 2. Description of S2 bands information

Bands	Spatial resolution (m)	Description	Central wavelength (nm)	Bandwidth (nm)
B2	10	Blue	0.496	65
B3	10	Green	0.560	35
B4	10	Red	0.664	30
B5	20	Red Edge1	0.703	15
B6	20	Red Edge2	0.740	15
B7	20	Red Edge3	0.782	20
B8	10	NIR	0.835	115
B8A	20	Red Edge4	0.864	20
B11	20	SWIR1	1.610	90
B12	20	SWIR2	2.202	180

NIR refers to near-infrared reflectance, while SWIR denotes short-wavelength InfraRed

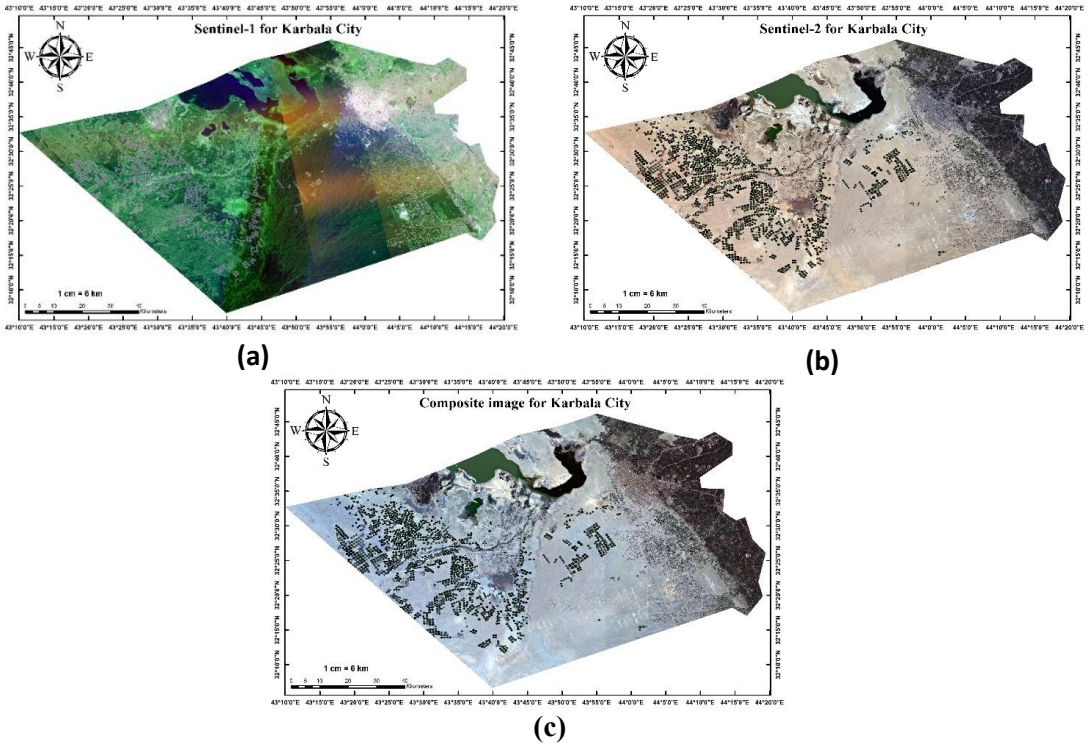

Fig.2 a. S1 image b. S2 image c. Composite S1 and S2 image

2.3. Training Samples

Our study used 5 main LULC classes: Water, Bareland, Vegetation, Palm, and Built-up Area, as shown in Table 3. To facilitate training and validation for the models, 60 training points gathered for every class, which decreased issues with class imbalance. Visual inspection of S1 and S2's temporal mix established the reference. A total of 300 training points were gathered.

Table 3. Description of five classes

Class ID.	Class	Description
0	Water	Water bodies include rivers, lakes, and reservoirs.
1	Bare land	Illustrate desert regions with less than 10% vegetation cover throughout the year.
2	Vegetation	Cropland and agriculture
3	Palm	Palm trees or woodland
4	Built-up	Parts representing buildings and urban land

2.4. Data Acquisition and Preprocessing Step

The S1 and S2 images time series acquired during the interested time and region go through multiple preprocessing steps to enhance image quality and usability. For S1 data starting from importing S1 GRD collection from ESA, these procedures include thermal noise removal, terrain correction, atmospheric correction, geometric rectification, and radiometric calibration. Following preprocessing, some necessary filters, which include selecting a range time of interest, filtering to obtain images with VH and VV dual polarization, filtering to acquire images gathered in interferometric wide swath mode (IW), and filtering based on the orbit descending or ascending mode. Then create a composite S1 image from means at various look angles and polarizations. For S2 (S2) data after being imported from ESA, some of the necessary filters applied to this collection, starting from selecting a range time of interest, a cloud masking technique as shown in Fig.3, conducted to eliminate unwanted pixels in the S2 image. The next step is to select the most significant spatial resolution bands 10 and 20 m. For this study, three spectral indices—NDVI, NDWI, and NDBI— calculated to extract spectral, textural, and contextual information, as illustrated in Fig.4, resulting in a composite image. The NDVI is commonly utilized to track variations in land cover and significantly improves the accuracy of classification, especially when used for the LULC classification. Calculated with the Red band (B4) and the Near-Infrared (NIR) band (B8). Water bodies in satellite imagery are highlighted by the NDWI, which is computed by the near-infrared (NIR) band (B8) and the green band (B3). Although the NDBI frequently improves built-up land information derived from remote sensing images, utilizing SWIR2 band (B12) and NIR band (B8) ratios with the right threshold setting can help recover impervious surfaces from urban areas. Table 4 shows the spectral indices equations. Finally, after all these preprocessing composites, S1 and S2 are combined to generate the final composite image.

Table 4. Spectral indices and the associated formula used in this study

Index	Formula	Author
NDVI	$\frac{B8 - B4}{B8 + B4}$	Rouse et al., 1973 (Rouse et al., 1974)
NDWI	$\frac{B3 - B8}{B3 + B8}$	McFeeters 1996 (McFEETERS, 1996)
NDBI	$\frac{SWIR2 - NIR}{SWIR2 + NIR}$	Zha, Y., et al., 2003 (Y. Zha and Ni, 2003)

3. METHODOLOGY

As illustrated in Fig.5, the proposed methodology is applied in the context of Al-Karbala City. The first step involves data acquisition and image Pre-processing. This encompasses retrieving composite satellite images from S1 and S2, and then the ROI mask was applied. The next step to generate the training samples on the composite image to be used in the analyses and

classification process. The next step encompasses the Zonal Statistics (ZS), and then predicts the five classes using an LSTM model. The Kappa coefficients and overall accuracy are calculated to evaluate the classification performance algorithm (Anokye et al., 2023).

(a) **(b)**

Fig. 3. Cloud masking technique applied on S2 image a. S2 image with cloud b. S2 image after applying cloud masking techniques

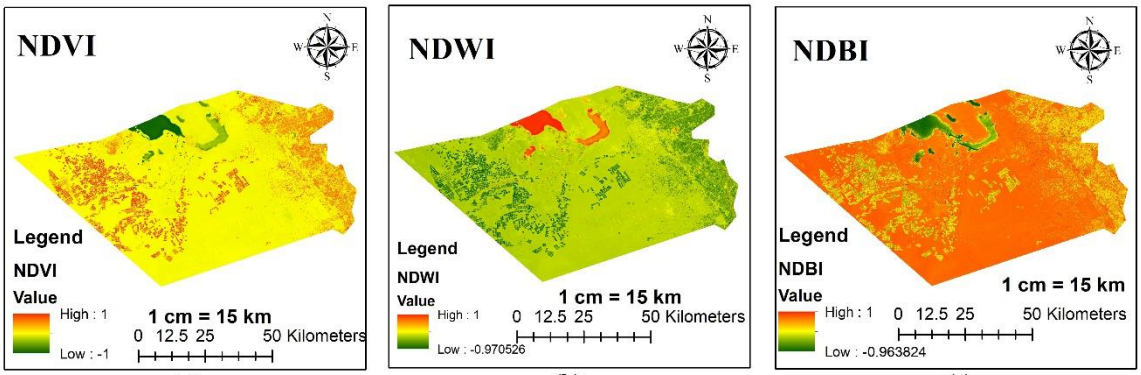

(a) **(b)** **(c)**

Fig. 4. a. NDVI for S2 b. NDWI for S2 c. NDBI for S2

3.1. Zonal Statistics Mechanism

The zonal statistics mechanism (ZS) is a valuable tool for categorizing and synthesizing several spatial data components in Remote Sensing analysis. This method is widely used in Remote Sensing to analyze spatial data. Usually, it entails evaluating raster-based datasets as zones defined by vector polygon areas, current raster areas, or other particular criteria such as watersheds, forest covers, or any land use type (Winsemius and Braaten, 2024).

Zonal statistics typically calculate statistical parameters such as mean, median, maximum, minimum, majority, minority, sum, standard deviation, and count of the pixels in each zone (Ashraf et al., 2024) for specific areas (buffers) based on the data values in those areas. Buffer zones are an essential element in spatial analyses to study interactions between geographical phenomena, such as the analysis of the impact of urban areas on vegetation.

Along with the quantitative summary, zonal statistics facilitate the identification of patterns, analysis of spatial distributions, and detection of hotspots or cold spots in the geographic areas of interest. For instance, they can identify regions of high population density in a city or areas with significant crop productivity in an agricultural field. However, these zones face a major challenge in the form of buffer contamination, as they contain a mixture of classes (such as

agricultural and urban lands), distorting the results and reducing the analysis's accuracy. The zonal statistics mechanism provides an advanced solution to this problem by identifying the dominant class within each buffer zone and excluding secondary classes, which enhances the reliability of spatial models. The coding of the data acquisition phase and the mechanism of zonal statistics are available at the following link: https://code.earthengine.google.com/f7df5d798433662bea4d83a475cedd23 .

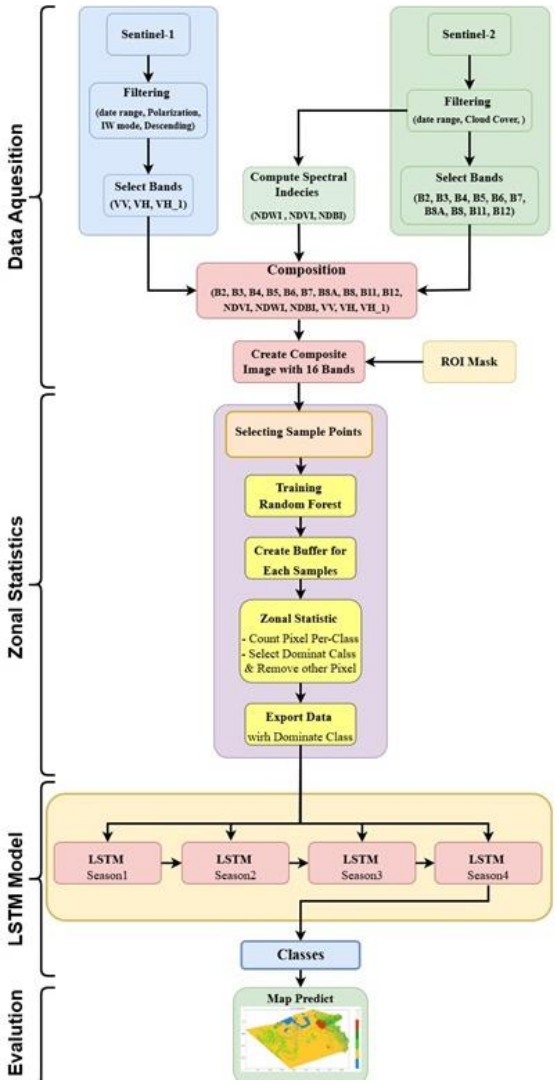

Fig. 5. Proposed system flowchart

The framework of this mechanism summarizes that when selecting sample points, an automated classification model (such as the Random Forest algorithm) is trained on the sample point data to ensure that each pixel in the image has a class (e.g., water, bare land, vegetation, palm, built-up). A circular buffer zone is created around each point at a specific distance (e.g., 50 km) to increase the training data. Each buffer zone is examined to determine if it contains more than one class, and buffer contamination is considered. The proportion of each class within each buffer contamination is determined by calculating the frequency histogram for each class.

Secondary classes are excluded, keeping only the dominant class with the highest frequency. Then, the data containing these dominant classes is extracted and exported to the LSTM network. Fig 6 illustrates the mechanism of the zonal statistics.

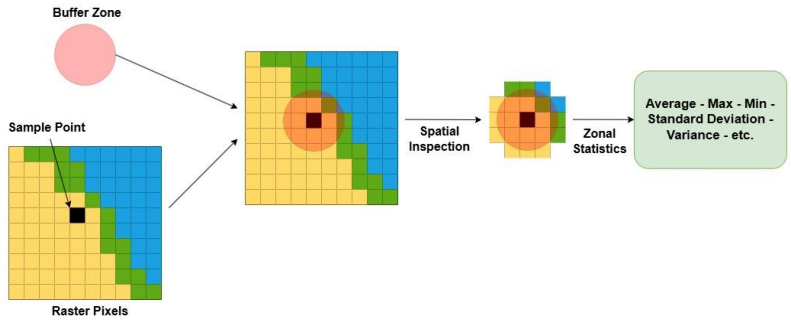

Fig. 6. Zonal Statistics Mechanism

3.2. Zonal Statistics Algorithm

Begin:

Inputs:

- Composite Satellite multi-band image of the GeoTIFF file (16 bands)
- Sample Points (total of 300 points, 60 per class)
- Class label (water, bareland, vegetation, palm, and build-up)

Output:

- CSV file of 11400 records with a class label for each season

Steps:

1: Sample Selection

- For each class $C_i \in \{0, 1, 2, 3, 4\}$ select 60 sample point
- Merge all points into a single Feature collection of 300 samples

2: Buffer creation

- For each sample point P_i :

  Create a circular buffer B_i with radius 100 meters

3: Zonal Statistics computation

- For each buffer B_i:
  - Using a frequency histogram, count the number of pixels per class within the buffer.
  - Identify the class with the highest pixel count → Dominant Class D_i
  - Remove all pixels in $\mathbf{B_i}$ that do not belong to $\mathbf{D_i}$

3: Data Extraction

- For each cleaned buffer $\mathbf{B_i}$:

  Extract pixel values (spectral bands values, class value)
  belong to the dominant class **Di**

4: Export Data

- Merge all extracted sample points into a single dataset
- Export the dataset as a CSV file

End

This method contributes to providing an innovative solution to the problem of buffer contamination by integrating remote sensing techniques with the Zonal Statistics mechanism, which enhances the quality of spatial analyses in environmental and urban studies. It also opens the door to broader climate change monitoring and calamity management applications, where choices are based on high-resolution spatial data.

3.3. Long Short-Term Memory (LSTM) Model

Among the several types of recurrent neural networks (RNNs) is LSTM. When the series of hidden states is designated as $\{h_1, h_2, \ldots, h_T\}$, an RRN can tackle the problem of problems involving sequential learning whereby the input sequence is represented by $\{x_1, x_2, \ldots, x_T\}$. With time expressed by t, the recurrent edge takes input given as x_t. For the time interval t-1, the preceding output value is denoted as h_{t-1}; thereafter, a weighted sum of output values follows. One can depict this via Equation 1.

$$h_t = \sigma (W_{hx}x_t + W_{hh}h_{t-1} + b) \quad (1)$$

W_{hx} shows the weights assigned to the input node and the hidden nodes in the recurrent layer; W_{hh} represents the weight pertaining to the previous time period and the recurrent hidden state node. Variable b represents the bias; variable σ establishes a non-linear activation function.

Nevertheless, training RNN models poses a challenge. As indicated in Equation 1, the endowment related to the recurrent invisible node is hm at time m. Whether $|W_{hh}|$ is less than 1 or more than 1, h_n might thus drift toward infinity or zero as n-m rises. The challenges of gradient disappearance and explosion, which might happen across different steps, are brought on by back-propagation faults. As a result, RNNs have difficulty learning long-range dependencies. LSTM replaces the recurrent hidden node with a memory cell to address the previously mentioned issues. The memory cell maintains a node with a constant weight and a self-connected recurrent edge, allowing the gradient to propagate over multiple time steps without diminishing or exploding. An LSTM primarily includes four parts: the input gate, forget gate, output gate, and candidate cell value. These elements streamline the computational process.

$$C_t\sim = tanh (W_{hC}.h_{t-1} + W_{xc}.x_t + b_c) \quad (2)$$

$$C_t = f_t \circ C_{t-1} + i_t \circ \quad (3)$$

$$O_t = \sigma (W_{ho}.h_{t-1} + W_{xo}.x_t + b_o) \quad (4)$$

$$h_t = O_t \circ tanh (C_t) \quad (5)$$

In this context, σ is represented as a logistic sigmoid function. Matrix multiplication is denoted by '.', while a dot product is indicated as '∘'. Bias terms include b_f, b_i, b_c, and b_o. Each weight matrix subscript has a specific meaning; for instance, the matrix for the hidden input gate is referred to as W_{hi}, while the matrix for the input–output gate is labeled W_{xo}.

3.4. Performance Evaluation

The model received one hundred epochs of training. Fig.7 presents the training and validation outcomes accuracy, while Fig.8 illustrates the levels of training and validation loss. The cross-class model performance metrics considered for this paper are shown in Table 5. The performance of the model for each class is shown in Table 6.

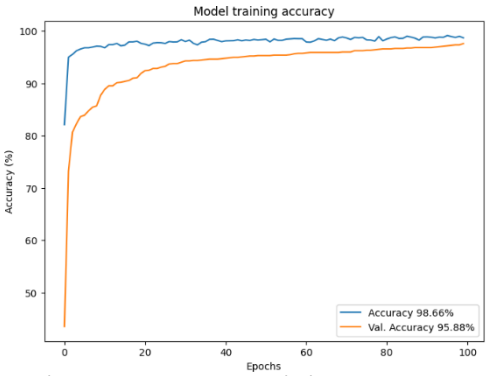

Fig. 7 The model training accuracy

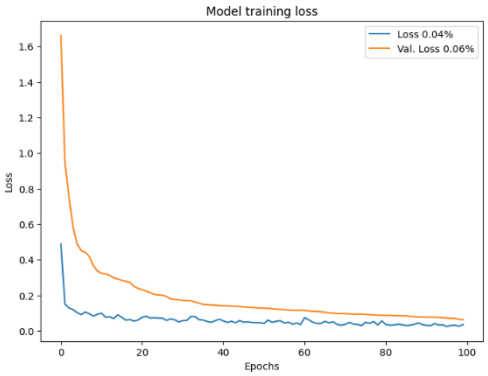

Fig. 8 The model training loss

Table 5. Cross-class model performance metrics

Metric	Value
Accuracy	0.9787
Precision	0.9768
Recall	0.9791
F1 Score	0.9775

Table 6. Per-class model performance metrics

Class	precision	recall	f1-score	support
Water	1.00	0.97	0.99	277
Bareland	0.92	1.00	0.96	196
Vegetation	0.99	0.96	0.97	229
Palm	1.00	0.99	0.99	263
Built-up	0.98	0.97	0.98	212

The model's Overall accuracy was 98.66%, and its validation accuracy was 95.88%. The training and validation loss values stood at 0.04 and 0.06, respectively. The Kappa coefficient was recorded at 96.75%. The convolution matrix shown in Fig.9 illustrates the capabilities of the actual class label to be predicted by the model. The model's ability to predict data that it does not observe during training is demonstrated by the resulting percentages for the classes Fig. 8b. The confusion matrix shows the machine learning model's classification accuracy in distinguishing five land classes: Water, Bare Land, Vegetation, Palm Trees, and Built-up. The numbers on the main diagonal (from top left to bottom right) represent correct classifications, while the numbers outside the diagonal indicate errors. For example, 270 water samples correctly classified, while 4 samples are mixed with built-up areas.

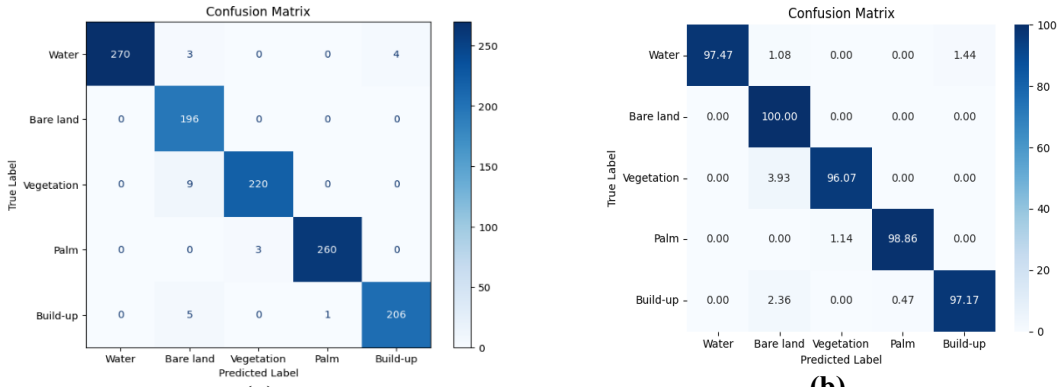

Fig. 9 a- The confusion matrix of classes. b- The confusion matrix of percentage of classes

4. RESULTS AND DISCUSSIONTS

Hardware components: The hardware used to develop and build the proposed model was a computer equipped with Intel Core i9 12th generation, with NVidia GeForce RTX 3060 with 8GB of RAM.

Software components: The software installed on this computer was:

1. Operating system: Microsoft Windows 11 Pro, 64-bit.
2. IDE: Visual Studio Code (for developing the proposed model.)
3. Google Earth Engine

The tested model was further evaluated on a 4-season satellite image to test its capability to predict the labels of seasonal imagery. Fig.10 shows the four input images used for evaluating the model.

The four images fed to the model to predict LULC. The resulting prediction is illustrated in Fig.11. Additionally, the percentage of land use distribution is illustrated in Fig. 11.

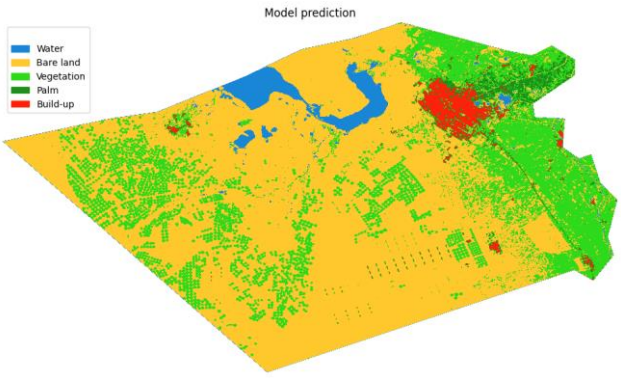

Fig. 11 The result map

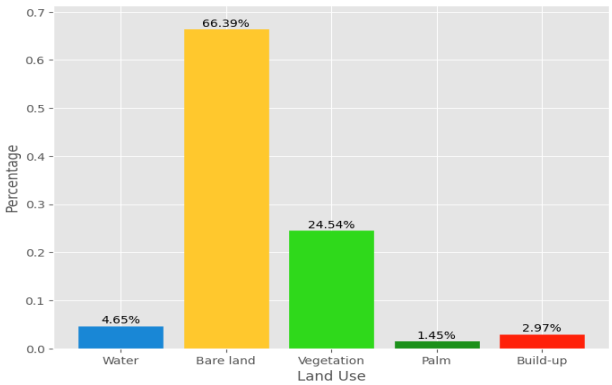

Fig. 12 The area of each class

Fig.12 shows the area of each class relative to the total area of Karbala city in the proposal model. Fig.13 shows an example of the proposed model's ability to predict buildings for the Sahara Karbala Company. The model can distinguish between the built-up and bare land classes despite the close color gradient between them.

Fig. 13 The prediction buildings for the Sahara Karbala Company

5. CONCLUSIONS

Land cover classification is a crucial process for providing valuable information to countries. The accuracy of this classification depends on the quality of the input data and training samples. To obtain comprehensive and integrated data, time series from the S1 and S2 satellites utilized, and spectral indices (NDVI, NDWI, and NDWB) were computed to create a combined image. This study introduced a new approach, different from previous research, to increase and enhance the quantity of data and training samples used by the model. The data was augmented by creating a buffer around each selected sample point. Zonal statistics then applied to avoid overlapping classes within a single buffer. Time series data extracted for the four seasons of 2024 in Karbala City utilized and input into an LSTM model. The results showed that the proposed model's classification accuracy surpassed that of earlier studies, which does not employ a zonal statistic mechanism, with overall accuracy and Kappa coefficient scores of 98.66% and 96.75%, respectively. A new model architecture, such as a convolutional neural network (CNN) or a hybrid model, could be considered for future work instead of using an LSTM network.

6. REFERENCES

Acharya, S., Hori, T. and Karki, S. (2023) ‘Assessing the spatio-temporal impact of landuse landcover change on water yield dynamics of rapidly urbanizing Kathmandu valley watershed of Nepal’, Journal of Hydrology: Regional Studies, 50, p. 101562. Available at: https://doi.org/10.1016/j.ejrh.2023.101562.

Almeida, C.A. de, Coutinho, A.C., Esquerdo, J.C. dalla M., Adami, M., Venturieri, A., Diniz, C.G., Dessay, N., Durieux, L. and Gomes, A.R. (2016) ‘High spatial resolution land use and land cover mapping of the Brazilian legal Amazon in 2008 using Landsat-5/TM and MODIS data’, Acta Amazonica, pp. 291–302. Available at: https://doi.org/10.1590/1809-4392201505504.

Alsraratee, Abdullah and Al-Azawei, A. (2025) 'CLASSIFYING ANDROID MALWARE CATEGORIES BASED ON DYNAMIC FEATURES: AN INTEGRATION OF FEATURE REDUCTION AND SELECTION TECHNIQUES', Kufa Journal of Engineering, 16(2), pp. 96–118. Available at: https://doi.org/10.30572/2018/KJE/160206.

Anokye, M., Cui, X., Yang, F., Wang, P., Sun, Y., Ma, H. and Amoako, E. (2023) 'Optimizing multi-classifier fusion for seabed sediment classification using machine learning', International Journal of Digital Earth, 17. Available at: https://doi.org/10.1080/17538947.2023.2295988.

Ashraf, T., Yin, F., Liu, L. and Zhang, Q. (2024) 'Land Subsidence Detection Using SBAS- and Stacking-InSAR with Zonal Statistics and Topographic Correlations in Lakhra Coal Mines, Pakistan', Remote Sensing, 16(20), p. 3815. Available at: https://doi.org/10.3390/rs16203815.

Bao, Y., Lin, L., Wu, S., Kwal Deng, K.A. and Petropoulos, G.P. (2018) 'Surface soil moisture retrievals over partially vegetated areas from the synergy of Sentinel-1 and Landsat 8 data using a modified water-cloud model', International Journal of Applied Earth Observation and Geoinformation, 72, pp. 76–85. Available at: https://doi.org/https://doi.org/10.1016/j.jag.2018.05.026.

Choudhury, U., Singh, S.K., Kumar, A., Meraj, G., Kumar, P. and Kanga, S. (2023) 'Assessing Land Use/Land Cover Changes and Urban Heat Island Intensification: A Case Study of Kamrup Metropolitan District, Northeast India (2000–2032)', Earth (Switzerland), 4(3), pp. 503–521. Available at: https://doi.org/10.3390/earth4030026.

Colson, D., Petropoulos, G.P. and Ferentinos, K.P. (2018) 'Exploring the Potential of Sentinels-1 & 2 of the Copernicus Mission in Support of Rapid and Cost-effective Wildfire Assessment', International Journal of Applied Earth Observation and Geoinformation, 73, pp. 262–276. Available at: https://doi.org/https://doi.org/10.1016/j.jag.2018.06.011.

Dagne, S.S., Hirpha, H.H., Tekoye, A.T., Dessie, Y.B. and Endeshaw, A.A. (2023) 'Fusion of sentinel-1 SAR and sentinel-2 MSI data for accurate Urban land use-land cover classification in Gondar City, Ethiopia', Environmental Systems Research, 12(1), p. 40. Available at: https://doi.org/10.1186/s40068-023-00324-5.

Erinjery, J.J., Singh, M. and Kent, R. (2018) 'Mapping and assessment of vegetation types in the tropical rainforests of the Western Ghats using multispectral Sentinel-2 and SAR Sentinel-1 satellite imagery', Remote Sensing of Environment, 216, pp. 345–354. Available at: https://doi.org/https://doi.org/10.1016/j.rse.2018.07.006.

H, S. (2024) 'CLOUD-SMART SURVEILLANCE: ENHANCING ANOMALY DETECTION IN VIDEO STREAMS WITH DF-CONVLSTM-BASED VAE-GAN', Kufa Journal of Engineering, 15(4), pp. 125–140. Available at: https://doi.org/10.30572/2018/KJE/150409.

Hu, B., Xu, Y., Wan, B., Wu, X. and Yi, G. (2018) 'Hydrothermally altered mineral mapping using synthetic application of Sentinel-2A MSI, ASTER and Hyperion data in the Duolong area, Tibetan Plateau, China', Ore Geology Reviews, 101, pp. 384–397. Available at: https://doi.org/https://doi.org/10.1016/j.oregeorev.2018.07.017.

Ienco, D., Gaetano, R., Dupaquier, C. and Maurel, P. (2017) 'Land Cover Classification via Multitemporal Spatial Data by Deep Recurrent Neural Networks', IEEE Geoscience and Remote Sensing Letters, 14(10), pp. 1685–1689. Available at: https://doi.org/10.1109/LGRS.2017.2728698.

Kother, S.H. and Obayes, H.K. (2025) 'Impact of Bands Number on LULC Classification Accuracy in Sentinel-2 Images BT - New Trends in Information and Communications Technology Applications', in A.M. Al-Bakry, M.A. Sahib, J.A. Aldhaibani, and A.N. Al-Shuwaili (eds). Cham: Springer Nature Switzerland, pp. 97–115.

Lunetta, R.S., Knight, J.F., Ediriwickrema, J., Lyon, J.G. and Worthy, L.D. (2006) 'Land-cover change detection using multi-temporal MODIS NDVI data', Remote Sensing of Environment, 105(2), pp. 142–154. Available at: https://doi.org/https://doi.org/10.1016/j.rse.2006.06.018.

Mahdianpari, M., Salehi, B., Mohammadimanesh, F., Homayouni, S. and Gill, E. (2019) 'The First Wetland Inventory Map of Newfoundland at a Spatial Resolution of 10 m Using Sentinel-1 and Sentinel-2 Data on the Google Earth Engine Cloud Computing Platform', Remote Sensing, 11(1). Available at: https://doi.org/10.3390/rs11010043.

McFEETERS, S.K. (1996) 'The use of the Normalized Difference Water Index (NDWI) in the delineation of open water features', International Journal of Remote Sensing, 17(7), pp. 1425–1432. Available at: https://doi.org/10.1080/01431169608948714.

Mohammed, H., Kareem, S. and Mohammed, A. (2022) 'A COMPARATIVE EVALUATION OF DEEP LEARNING METHODS IN DIGITAL IMAGE CLASSIFICATION', Kufa Journal of Engineering, 13(4), pp. 53–69. Available at: https://doi.org/10.30572/2018/KJE/130405.

Nigar, A., Li, Y., Jat Baloch, M.Y., Alrefaei, A.F. and Almutairi, M.H. (2024) 'Comparison of machine and deep learning algorithms using Google Earth Engine and Python for land

classifications', Frontiers in Environmental Science, 12. Available at: https://doi.org/10.3389/fenvs.2024.1378443.

Phan, T.N., Kuch, V. and Lehnert, L.W. (2020) 'Land Cover Classification using Google Earth Engine and Random Forest Classifier—The Role of Image Composition', Remote Sensing, 12(15). Available at: https://doi.org/10.3390/rs12152411.

Rajendran, G.B., Kumarasamy, U.M., Zarro, C., Divakarachari, P.B. and Ullo, S.L. (2020) 'Land-Use and Land-Cover Classification Using a Human Group-Based Particle Swarm Optimization Algorithm with an LSTM Classifier on Hybrid Pre-Processing Remote-Sensing Images', Remote Sensing, 12(24), p. 4135. Available at: https://doi.org/10.3390/rs12244135.

Roteta, E., Bastarrika, A., Padilla, M., Storm, T. and Chuvieco, E. (2019) 'Development of a Sentinel-2 burned area algorithm: Generation of a small fire database for sub-Saharan Africa', Remote Sensing of Environment, 222, pp. 1–17. Available at: https://doi.org/10.1016/j.rse.2018.12.011.

Rouse, J.W., Haas, R.H., Schell, J.A., Deering, D.W. and others (1974) 'Monitoring vegetation systems in the Great Plains with ERTS', NASA Spec. Publ, 351(1), p. 309.

Ruzza, G., Guerriero, L., Grelle, G., Guadagno, F.M. and Revellino, P. (2019) 'Multi-Method Tracking of Monsoon Floods Using Sentinel-1 Imagery', Water, 11(11). Available at: https://doi.org/10.3390/w11112289.

Sannigrahi, S., Bhatt, S., Rahmat, S., Paul, S.K. and Sen, S. (2018) 'Estimating global ecosystem service values and its response to land surface dynamics during 1995–2015', Journal of Environmental Management, 223, pp. 115–131. Available at: https://doi.org/https://doi.org/10.1016/j.jenvman.2018.05.091.

Santos, L.A., Ferreira, K.R., Camara, G., Picoli, M.C.A. and Simoes, R.E. (2021) 'Quality control and class noise reduction of satellite image time series', ISPRS Journal of Photogrammetry and Remote Sensing, 177, pp. 75–88. Available at: https://doi.org/https://doi.org/10.1016/j.isprsjprs.2021.04.014.

Shorten, C. and Khoshgoftaar, T.M. (2019) 'A survey on Image Data Augmentation for Deep Learning', Journal of Big Data, 6(1), p. 60. Available at: https://doi.org/10.1186/s40537-019-0197-0.

Tejasree, G. and Agilandeeswari, L. (2024) 'Land use/land cover (LULC) classification using deep-LSTM for hyperspectral images', The Egyptian Journal of Remote Sensing and Space

Sciences, 27(1), pp. 52–68. Available at: https://doi.org/https://doi.org/10.1016/j.ejrs.2024.01.004.

Wang, S., Ma, Q., Ding, H. and Liang, H. (2018) 'Detection of urban expansion and land surface temperature change using multi-temporal landsat images', Resources, Conservation and Recycling, 128, pp. 526–534. Available at: https://doi.org/https://doi.org/10.1016/j.resconrec.2016.05.011.

Winsemius, S. and Braaten, J. (2024) 'Zonal Statistics', Cloud-Based Remote Sensing with Google Earth Engine, pp. 463–485. Available at: https://doi.org/10.1007/978-3-031-26588-4_24.

Y. Zha, J.G. and Ni, S. (2003) 'Use of normalized difference built-up index in automatically mapping urban areas from TM imagery', International Journal of Remote Sensing, 24(3), pp. 583–594. Available at: https://doi.org/10.1080/01431160304987.

Yassine, H., Tout, K. and Jaber, M. (2021) 'IMPROVING LULC CLASSIFICATION FROM SATELLITE IMAGERY USING DEEP LEARNING – EUROSAT DATASET', The International Archives of the Photogrammetry, Remote Sensing and Spatial Information Sciences, XLIII-B3-2, pp. 369–376. Available at: https://doi.org/10.5194/isprs-archives-XLIII-B3-2021-369-2021.

Zhang, H., Li, J., Wang, T., Lin, H., Zheng, Z., Li, Y. and Lu, Y. (2018) 'A manifold learning approach to urban land cover classification with optical and radar data', Landscape and Urban Planning, 172, pp. 11–24. Available at: https://doi.org/https://doi.org/10.1016/j.landurbplan.2017.12.009.

Zurqani, H., Albukhari, A., Al Daikh, A.S., Elfadli, K. and Bataw, A. (2022) 'Geospatial Mapping and Analysis of the 2019 Flood Disaster Extent and Impact in the City of Ghat in Southwestern Libya Using Google Earth Engine and Deep Learning Technique', in. Available at: https://doi.org/10.1007/978-3-030-97810-5_10.